Rayleigh-Taylor-induced magnetic fields in laser-irradiated plastic foils

M. J.-E. Manuel, C. K. Li, F. H. Séguin, J. A. Frenje, D. T. Casey et al.

Related Articles

Dust-acoustic waves and stability in the permeating dusty plasma. II. Power-law distributions
Phys. Plasmas 19, 083706 (2012)

The internal disruption as hard Magnetohydrodynamic limit of 1/2 sawtooth like activity in large helical device
Phys. Plasmas 19, 082512 (2012)

Non-modal analysis of the diocotron instability: Plane geometry
Phys. Plasmas 19, 082112 (2012)

Verification and validation of linear gyrokinetic simulation of Alfvén eigenmodes in the DIII-D tokamak
Phys. Plasmas 19, 082511 (2012)

The effects of nonthermal electron distributions on ion-temperature-gradient driven drift-wave instabilities in electron-ion plasma
Phys. Plasmas 19, 082111 (2012)
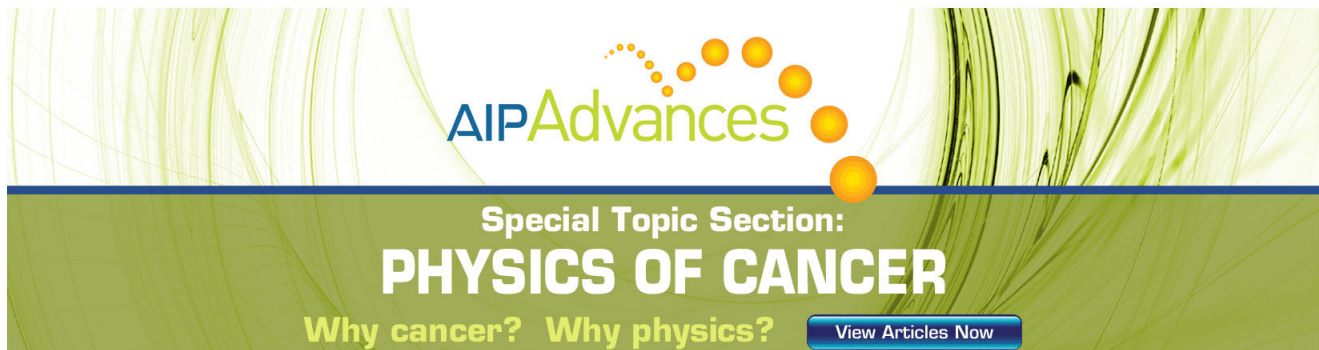
Additional information on Phys. Plasmas

Journal Homepage: http://pop.aip.org/

Journal Information: http://pop.aip.org/about/about_the_journal

Top downloads: http://pop.aip.org/features/most_downloaded

Information for Authors: http://pop.aip.org/authors

Rayleigh-Taylor-induced magnetic fields in laser-irradiated plastic foils

M. J.-E. Manuel,[1] C. K. Li,[1] F. H. Séguin,[1] J. A. Frenje,[1] D. T. Casey,[1] R. D. Petrasso,[1]
S. X. Hu,[2] R. Betti,[2,a)] J. Hager,[2,b)] D. D. Meyerhofer,[2,a)] and V. Smalyuk[2,c)]

[1]*Massachusetts Institute of Technology, Cambridge, Massachusetts 02139, USA*
[2]*Laboratory for Laser Energetics, University of Rochester, Rochester, New York 14623, USA*

Experimental observations of magnetic fields generated by Rayleigh-Taylor growth in laser-irradiated planar foils are presented. X-ray and monoenergetic proton radiographic techniques were used to probe plastic foils with seeded surface perturbations at different times during the evolution. Protons deflected by fields in the target cause modulations in proton fluence at the seed wavelength of 120 μm. Path-integrated magnetic-field strengths were inferred from modulations in proton fluence using a discrete-Fourier-transform analysis technique and found to increase from 10 to 100 T-μm during linear growth. Electron thermal conduction was shown to be unaffected by Rayleigh-Taylor-induced magnetic fields during the linear growth phase. © *2012 American Institute of Physics.* [http://dx.doi.org/10.1063/1.4748579]

I. INTRODUCTION

The Rayleigh-Taylor[1,2] (RT) instability is a concern for capsule integrity in inertial confinement fusion (ICF).[3] In the classic, stratified-fluid problem, the RT instability occurs when a high-density fluid is supported against acceleration by a lower-density fluid. For small amplitude perturbations at a single wavelength ($\lambda = 2\pi/k$), the growth rate at the interface of these fluids is $\gamma = \sqrt{A_t a k}$, where A_t is the Atwood number and a is the acceleration.[1,2] In laser-matter interactions, as seen in inertial confinement fusion, a continuous density profile is created whereby the residual mass is accelerated by the lighter, expanding plasma, forming an RT-unstable region near the ablation front.

During linear growth, perturbations on the ablation surface grow approximately exponentially ($h(t) \approx h_0 e^{\gamma_{RT} t}$) until reaching the saturation point when $h \approx \lambda/10$, thereafter growing at a slower rate.[4] The ablative nature of the RT-instability in laser-produced plasmas has been predicted,[5–7] and verified[8–10] to have a stabilizing effect on the linear growth rate. For an ablatively driven target $A_t \approx 1$ and the linear growth rate is[5]

$$\gamma_{RT} = \sqrt{\frac{ka}{1 + kL_\rho}} - \beta k V_a \,, \qquad (1)$$

where L_ρ is the density scale length, β is the ablative stabilization coefficient ($\beta \approx 3$ for direct-drive[5,11]), and V_a is the ablation velocity. The ablative, linear growth rate illustrates that perturbations with wavelengths smaller than $\lambda \approx 2\pi\beta^2 V_a^2/a$ ($\sim$1-10 μm for typical parameters) are linearly stable. The fluids involved with an ablatively driven target are not charge-neutral, but are plasmas consisting of separate populations of ions and electrons.

During the ablation process, dynamic charge separation and subsequent current generation can create magnetic fields within the plasma.[12,13] By comparing the magnetic energy density with energy in fluid vorticity, the formulation of Evans[14] demonstrated that for an RT-unstable plastic (CH)[15] plasma, growth rates of wavelengths less than $\sim$5 μm would be affected by self-generated magnetic fields. Experiments discussed herein examined wavelengths larger ($\lambda \sim 120$ μm) than those affected by magnetic fields. Furthermore, in laser-ablation systems, the growth rate given in Eq. (1) shows that small wavelengths, which may be affected by magnetic fields, are ablatively stabilized. Even though magnetic fields may not play an important role during linear growth of relevant wavelengths, they may potentially affect energy transport from the under-dense plasma to the ablation surface.

To drive a target through the ablation process, as in inertial fusion, energy must be efficiently deposited to the ablation surface. Energy provided by thermal electrons is conducted through the over-dense region to the ablation surface as illustrated in Figure 1. Acceleration of ablated target material into the over-dense plasma generates an RT-unstable region because of the large, acceleration-opposing density gradient. Surface perturbations on the target grow because of this instability and induce magnetic fields. The electron thermal conduction across a magnetic field ($\kappa_\perp$) is reduced from the classical value ($\kappa_\parallel$) as

$$\frac{\kappa_\perp}{\kappa_\parallel} = \frac{\gamma_1' \chi^2 + \gamma_0'}{\gamma_0(\chi^4 + \delta_1 \chi^2 + \delta_0)} \,, \qquad (2)$$

where the coefficients $\gamma_1', \gamma_0', \gamma_0, \delta_1, \delta_0$ are given by Braginskii.[16] The Hall parameter χ is a quantity describing the characteristic number of cycles a thermal electron makes about a magnetic-field line before undergoing a collision. This quantity can be expressed as $\chi = \omega_{ce}\tau_{ei}$, where ω_{ce} and τ_{ei} are the
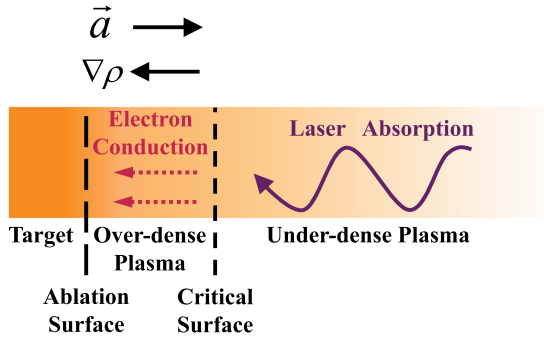
FIG. 1. Schematic drawing of laser-foil interactions with important regions labeled. The ablation front is unstable to RT growth because the acceleration is in the opposite direction of the density gradient.

electron cyclotron frequency and characteristic collision time, respectively. The Hall parameter can be expressed in relevant units by,

$$\chi \approx 20 \frac{B T_e^{3/2}}{Z n_e \ln \Lambda}, \qquad (3)$$

where B is in Tesla, the electron temperature T_e is in keV, density n_e is in 10^{20} cm^{-3}, Z is the average ionization state, and $\ln \Lambda$ is the Coulomb logarithm. The Hall parameter characterizes the reduction in thermal conduction due to magnetic fields. A Hall parameter value as small as ~0.3 will reduce thermal conduction to ~40 % of the classical value in a CH plasma under typical conditions.

RT-unstable plasma configurations occur in many systems: in laser-matter interactions,[10] during the acceleration and deceleration phases in inertial confinement fusion,[17] during core-collapse of supernovae,[18] in stellar coronae,[19] and in other astrophysical phenomena.[20] The so-called Biermann battery[21] is the dominant source of self-generated magnetic fields in plasmas. This source term has been predicted to cause field generation due to the RT instability in astrophysical contexts[22] as well as in laser-plasma interactions.[23] Mima *et al.*[24] and Nishiguchi *et al.*[25] investigated different

models and environments for magnetic field generation, but both predicted peak field strengths on the order of ~10-100 T. Fields of this magnitude near the critical surface in directly driven ICF capsules can drastically affect electron thermal conduction and inhibit effective ablative drive.

The work discussed herein extends previously reported experiments[26] to study RT-induced magnetic fields in laser-driven planar targets. Experimental configurations of both x-ray and proton radiography are discussed in Sec. II. Plasma evolution using the 2-D hydrodynamic code DRACO[27] is demonstrated in Sec. III and an overview on electromagnetic field generation is given in Sec. IV with particular attention paid to RT-induced field structure. The discrete-Fourier-transform (DFT) technique implemented to analyze these data is discussed in Sec. V. Experimental results of path-integrated fields during linear growth are presented in Sec. VI and subsequent field magnitude estimates are discussed in Sec. VII. This paper concludes with a summary of the results presented and future directions of this work in Sec. VIII.

II. PROTON AND X-RAY RADIOGRAPHY

Both proton and x ray radiography experiments were performed on the OMEGA laser[28] using the setups shown in Figures 2(a)–2(c) and Figures 2(d)–2(f), respectively. Imaging protons are sensitive to both areal density and electromagnetic fields such that fluence modulations in proton radiographs are due to a combination of these effects, as illustrated in Figures 2(b) and 2(c). The primary goal of these experiments was to relate proton fluence modulations, and therefore deflections, to path-integrated field strengths. For a complete experimental picture, independent measurements of areal density modulations were made using well established[10,29] x ray radiographic techniques.

X ray radiographs provided measurements of density-modulation growth in the target. Face-on images were obtained using ~1.3 keV x rays from a uranium backlighter and a streak camera[10,29] having a temporal resolution of
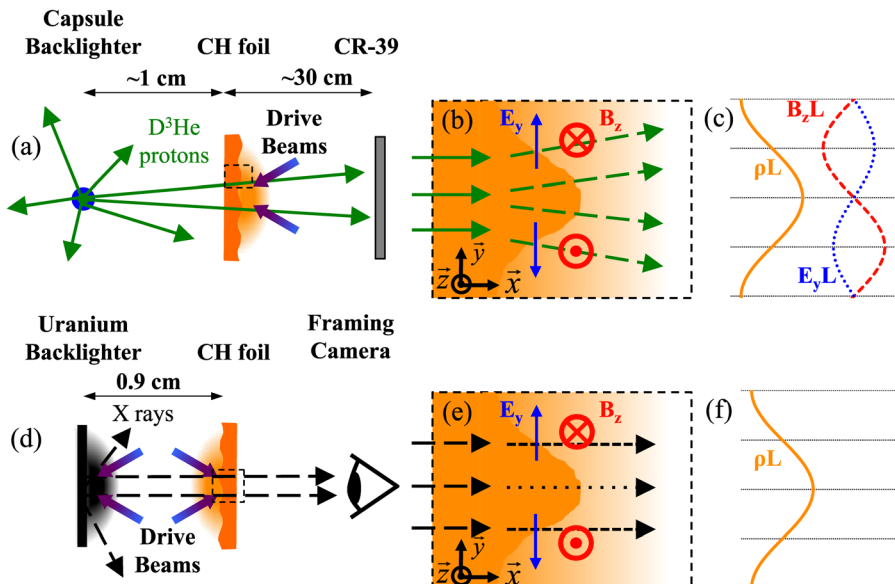

FIG. 2. (a) A schematic drawing of the experimental setup used to radiograph directly-driven plastic (CH) foils. Proton images are recorded on CR-39 nuclear track detectors. (b) An expanded view of proton (green) deflections due to RT-induced density, E field (blue), and B field (red) modulations in the target. (c) Proton-sensitive, path-integrated quantities (arbitrary units) are shown during the linear growth phase. (d) A schematic drawing of the experimental setup for x ray radiography of CH foils. A uranium foil backlighter was used, and images taken on film. (e) An expanded view of x ray interaction with the laser-irradiated target; x rays are attenuated more through RT spikes than through bubbles. (f) X rays are sensitive only to the areal density.

~80 ps and a spatial resolution of ~10 μm. Streaked images were recorded on Kodak T-Max 3200 film and digitized using a Perkins-Elmer PDS microdensitometer.[30] Under these experimental conditions, the optical depth measured (OD) may be converted to an areal density by $\rho L = OD/\mu_U$, where the conversion factor for uranium and the equipment used has been calculated as $\mu_U \approx 0.95$ cm^2/mg, such that ρL is in mg/cm^2. These measurements provide direct experimental data on the growth rate of areal density modulations in these laser-irradiated foils.

Monoenergetic proton radiography[31,32] was used to probe RT-induced field structures. A ~2 μm-thin-glass, exploding pusher filled with 18 atm of equimolar D^{3}He gas was imploded by up to 20 OMEGA laser beams. This backlighting technique provides a quasi-isotropic,[33] monoenergetic (~15 MeV) proton source with an approximately Gaussian emission profile with a FWHM of ~45 μm and burn duration of ~150 ps, as demonstrated in many experiments.[34–37] Imaging protons were incident on 10 cm × 10 cm CR-39 detectors that were filter-matched to range ~15 MeV protons down to ~4 MeV, where CR-39 has 100% detection efficiency.[38] After exposure, the CR-39 was processed in 6 N NaOH solution to reveal tracks left by the protons. Each piece of CR-39 was scanned using a digital optical-microscope system and individual track locations and characteristics were retained by the system for analysis.[38]

Foil surfaces were either flat or seeded with ridge-like 2-D sinusoidal modulations. The exact laser configuration was not constant across all experiments, however, drive characteristics were nominally equal. The laser drive in all cases was a 2 ns square pulse with a total of ~3300 J of energy on-target. All drive beams implemented SG4 distributed phase plates[39] (DPPs) to provide a ~750 μm diameter spot and a drive intensity of I $\lesssim 4 \times 10^{14}$ W/cm^2. The beams were smoothed by spectral dispersion[40] (SSD) and distributed polarization rotators[41] (DPRs). In proton radiography experiments, CH foils and CR-39 detectors were located ~1 cm and ~30 cm from the backlighter, respectively, providing a magnification of M ~ 30. The strength of path-integrated mass and fields, as illustrated in Figure 2(c), in conjunction with the optical geometry determines the amount of proton deflection.

The quasi-uniform[33] flux of protons provided by the backlighter is perturbed through inhomogeneous mass distributions and electromagnetic fields in the plasma. Modulations in proton flux are caused by deflections perpendicular to proton trajectories. The amount of deflection undergone by a particle caused by B or E fields is proportional to the path-integrated field strength

$$\theta_B = \frac{q}{\sqrt{2m_p E_p}} \int B_\perp \, dl, \qquad (4)$$

$$\theta_E = \frac{q}{2E_p} \int E_\perp \, dl, \qquad (5)$$

where q is the particle charge, m_p the particle mass, and E_p the particle energy. $B_\perp$ and $E_\perp$ are the magnetic- and electric-field magnitudes perpendicular to the particle trajec-

tory, respectively. Information about the path-integrated field strength is encoded within proton fluence modulations. RT-induced modulations cause local broadening of the proton fluence due to Coulomb scattering and the Lorentz force, as illustrated in Figure 2(b). The total fluence modulation is due to a combination of perturbing effects from both field deflections and Coulomb scattering.

III. MODELING PLASMA EVOLUTION

The radiation-hydrodynamic code DRACO[27,42] was used to model laser-foil interactions in these experiments. These calculations were done in 2-D to self-consistently evolve the foil hydrodynamics, though no electric or magnetic fields were included. The no-field approximation is typically sufficient for predicting the hydrodynamics in these types of plasmas[10,43] due to the high ratio of plasma pressure to magnetic pressure ($\beta = 2\mu_0 p/B^2 \gtrsim 10^4$ under typical conditions).

Laser-foil interactions were simulated with DRACO using a 2-D cylindrical geometry, assuming azimuthal symmetry. These calculations were done after the experiments and implemented the incident angles and energies for individual beams in a super-Gaussian beam spot for the fielded SG4 DPPs. Beams were incident onto a 21-μm thick CH foil with sinusoidal perturbations of wavelength 120 μm and initial amplitude of 0.27 μm. The beams were azimuthally symmetric and irradiated the CH foil on axis. A constant flux limiter[44] of $f = 0.06$ was implemented in these calculations which has previously been shown[10] to reproduce drive conditions well at intensities below ~5×10^{14} W/cm^2.

The predicted hydrodynamic results are shown in Figure 3 for three sample times during the 2 ns laser pulse. One-dimensional quantities were obtained by averaging over 120 μm (a single wavelength) in radius and plotted as a function of distance on-axis and illustrated in the left column of Figure 3. In these plots, the lasers were incident from the right and the ablation (Abl.), critical (Crit.), and quarter critical (Quart. Crit.) surfaces are labeled for reference. The bulk of the foil is clearly shown by the density-peak on the left side of each plot and is observed to move towards the left. The maximum density was calculated to be ~2.5 g/cm^3 indicating a ~2.5 compression factor. An approximately constant mass ablation rate was calculated as $\dot{m} \approx 4 \times 10^5$ g/cm^2/s, corresponding to an ablation velocity of $V_a \sim 2$ μm/ns. In the reference frame of the ablation front, the acceleration is directed toward the right and the density gradient towards the left, generating an RT unstable region.

Two-dimensional contours of electron density (solid) and temperature (long dash) are plotted in the column on the right of Figure 3 corresponding to the three sample times. Peak number density contours were set to 2.5×10^{23} cm^{-3} (~0.8 g/cm^3) and are highlighted by thicker solid (orange) lines in each plot. The number density contours decrease by increments of 8×10^{22} cm^{-3}, such that the short-dashed line on the far right within each plot is at 10^{22} cm^{-3} (approximately the critical density). Electron temperature contours are labeled and shown to sharply increase
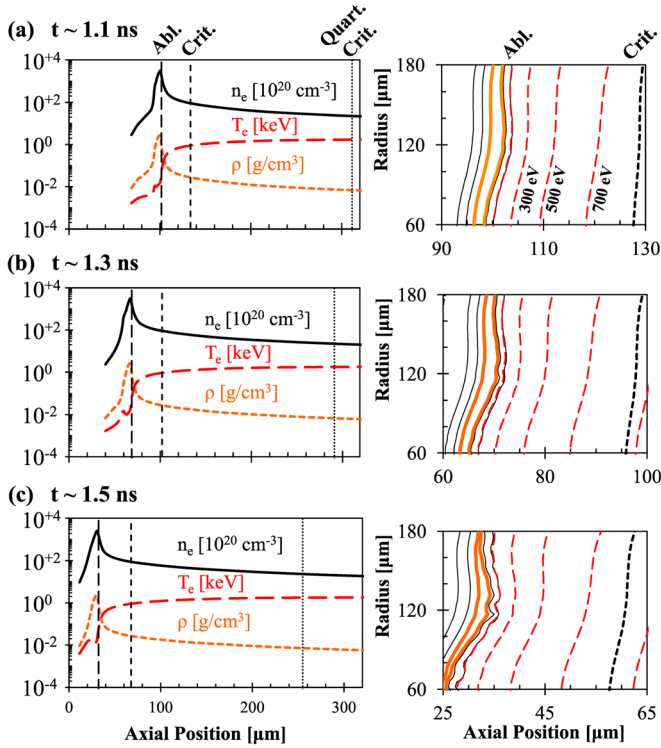
FIG. 3. Predictions from the DRACO simulation for three sample times. (left column) (a)–(c) Fluid density (short dash), electron number density (solid), and electron temperature (long dash) were averaged in "radius" to provide 1-D profiles along the axis (lasers come in from the right). (right column) (a)–(c) Corresponding 2-D electron number density (solid) and temperature (long dash) contours are shown up to the critical surfaces (short dash) at each time: (a) 1.1 ns, (b) 1.3 ns, (c) 1.5 ns after drive laser onset. The peak number density contours (thick solid) were set to 2.5×10^{23} cm^{-3} and subsequent contours (thin solid) decrease incrementally by 8×10^{22} cm^{-3}.

from the ablation front to the critical surface. Additionally, Rayleigh-Taylor growth of the sinusoidal surface perturbation is clearly illustrated by the growing amplitude of the peak density contours.

IV. ELECTROMAGNETIC FIELDS IN PLASMA

Self-generated, electromagnetic fields have been observed[12,13,35,45] in many laser-produced plasmas. Electric-field generation occurs primarily in response to gradients in the electron pressure, whereas the dominant source of self-generated magnetic fields is related to perpendicular gradients in the electron temperature and density. Figures 3(a)–3(c) show the large gradients along the foil normal due to the ablation process. Rayleigh-Taylor growth provides gradients perpendicular to the foil normal, thereby generating noncollinear temperature and density gradients to generate magnetic fields. Sections IV A and IV B provide a brief overview of the mechanisms involved in self-generated electromagnetic fields and concludes with ideal magnetohydrodynamic (MHD) calculations of post-processed DRACO simulations.

A. Electric field generation

Electrical shielding occurs in plasmas due to the high mobility of electrons. In a uniform plasma Debye shielding of positively charged ions screens electric fields with scale size

$L_E > \lambda_D$, where λ_D is the local, electron Debye length. Debye shielding neutralizes individual charges and characterizes the quasi-neutrality of the plasma. This allows for the collective behavior to dominate over small-scale Coulombic effects.

Long scale-length charge separation, however, can generate electric fields inside plasmas. In typical laser-produced plasmas, the Debye length is much smaller ($\sim$nm) than other scale lengths of interest ($\sim\mu$m). The investigation of electric field generation begins with the electron momentum equation, with electron inertia ignored on hydrodynamic time scales, such that $m_e \to 0$ and it is recognized that viscosity is dominated by ion motion, so electron viscosity is neglected. This results in the formulation presented by Braginksii,[16]

$$\mathbf{E} \approx -\frac{\nabla p_e}{e_0 n_e} - \mathbf{V}_e \times \mathbf{B} + \frac{\mathbf{R}_e}{e_0 n_e} , \qquad (6)$$

where p_e, n_e, and e_0 are the electron pressure, number density, and charge, respectively. Collisional effects are contained within $\mathbf{R}_e$ and $\mathbf{V}_e$ is the bulk electron fluid velocity. To understand the basic generation mechanisms, dissipative effects due to collisions are ignored forming the ideal MHD equation for E-fields,

$$\mathbf{E} \approx -\frac{\nabla p_e}{e_0 n_e} - \mathbf{V}_e \times \mathbf{B} . \qquad (7)$$

Long scale-length electric fields are mainly generated in response to the electron pressure gradient[12,13,16] with an additional component due to the collisionless Hall effect. In the isothermal case, electric field generation is simply dependent on the electron temperature and density scale length, increasing in strength as the gradient steepens.

B. Magnetic field generation

Unlike electric fields, magnetic fields are not shielded by electron screening effects and can dramatically affect plasma dynamics. Using Eq. (6) and Faraday's Law, the equation governing magnetic field evolution is given by

$$\frac{\partial \mathbf{B}}{\partial t} \approx \nabla \times \left(\frac{\nabla p_e}{e_0 n_e} + \mathbf{V}_e \times \mathbf{B} - \frac{\mathbf{R}_e}{e_0 n_e} \right) . \qquad (8)$$

In its typical form,[13,16] the electron fluid velocity is replaced by the ion fluid velocity $\mathbf{V}_i$ and current density $\mathbf{j} = e_0 n_e (\mathbf{V}_i - \mathbf{V}_e)$. With these substitutions, the general form for magnetic field evolution in a plasma becomes

$$\frac{\partial \mathbf{B}}{\partial t} \approx \nabla \times \left(\underbrace{\frac{\nabla p_e}{e_0 n_e}}_{(a)} + \underbrace{\mathbf{V}_i \times \mathbf{B}}_{(b)} - \underbrace{\frac{\mathbf{j}}{e_0 n_e} \times \mathbf{B}}_{(c)} - \underbrace{\frac{\mathbf{R}_e}{e_0 n_e}}_{(d)} \right) . \qquad (9)$$

Each term is described as follows: (a) the Biermann battery[21] or thermo-electric[13] term, (b) the dynamo or fluid convection term, (c) the collisionless Hall term, and (d) the collisional terms.

Magnetic field generation in plasmas is a rich and complex topic that has been investigated by many.[13,16,31,46] Within the collisional terms, various diffusion, convection,

and field generation sources exist (including the well known Nernst convection[47]) that are described by Haines.[13] Magnetic field *generation* is largely dominated by sources due to the gradient of the isotropic electron pressure, which is the foundation of estimating field strengths and structures. To derive the well known Biermann battery source term, convection, diffusion, and collisional effects are ignored, and the isotropic pressure gradient, (a) in Eq. (9), is shown to be the primary source of self-generated magnetic fields. Using the standard definition of the electron pressure as $p_e = n_e T_e$, this thermo-electric source term is driven by non-collinear temperature and density gradients

$$\frac{\partial \mathbf{B}}{\partial t} \approx \frac{\nabla T_e \times \nabla n_e}{e_0 n_e}.$$ (10)

Though this formulation is not very accurate, it serves to illustrate the primary *generation* mechanism.

The first step to a more tractable model for magnetic field evolution is to note that the collisionless Hall term is second order in **B** and can thus be neglected in comparison to other terms. If the ideal, collisionless, limit is taken, the magnetic field evolution can be simplified to,

$$\frac{\partial \mathbf{B}}{\partial t} \approx \nabla \times \left(\frac{\nabla p_e}{e_0 n_e} \right) + \nabla \times (\mathbf{V}_i \times \mathbf{B}).$$ (11)

Equation (11) is similar to that of fluid vorticity in an inviscid fluid,[14,15]

$$\frac{\partial \boldsymbol{\xi}}{\partial t} \approx -\nabla \times \left(\frac{\nabla p}{\rho} \right) + \nabla \times (\mathbf{V} \times \boldsymbol{\xi}),$$ (12)

where $\boldsymbol{\xi} = \nabla \times \mathbf{V}$ is the fluid vorticity, $\mathbf{V} = \mathbf{V}_i$ is the fluid velocity, $p = p_e + p_i$ is the total pressure, and $\rho = m_i n_i$ is the fluid density. Assuming that $T_e \approx T_i$, it may be easily verified that the magnetic field can be written,[14]

$$\mathbf{B} \approx \frac{-m_i}{e_0(Z+1)} \boldsymbol{\xi}.$$ (13)

Equation (13) illustrates that magnetic fields are proportional to the fluid vorticity in the ideal MHD limit. In many cases, the resistivity is not negligible and, in some instances, the Nernst effect,[47] caused by the collisional thermal force $\mathbf{R}_T$, must be included; the effect of these terms will be discussed in Sec. VII.

Hydrodynamic results predicted from DRACO were post-processed using Eqs. (7) and (13) to calculate magnetic- and electric-field structure under these experimental conditions. Figures 4(a)–4(c) illustrate the ideal MHD electromagnetic field structures generated by the plasma for the same sample times as shown in Figure 3. During linear growth, sinusoidal surface perturbations lead to sinusoidal fields, as expected. These calculations indicate that fields begin within a narrow space near the ablation surface, then grow and expand toward the critical surface in time. This work demonstrates a technique to measure the sinusoidal fields caused by the Biermann-battery source generated during linear RT-growth.
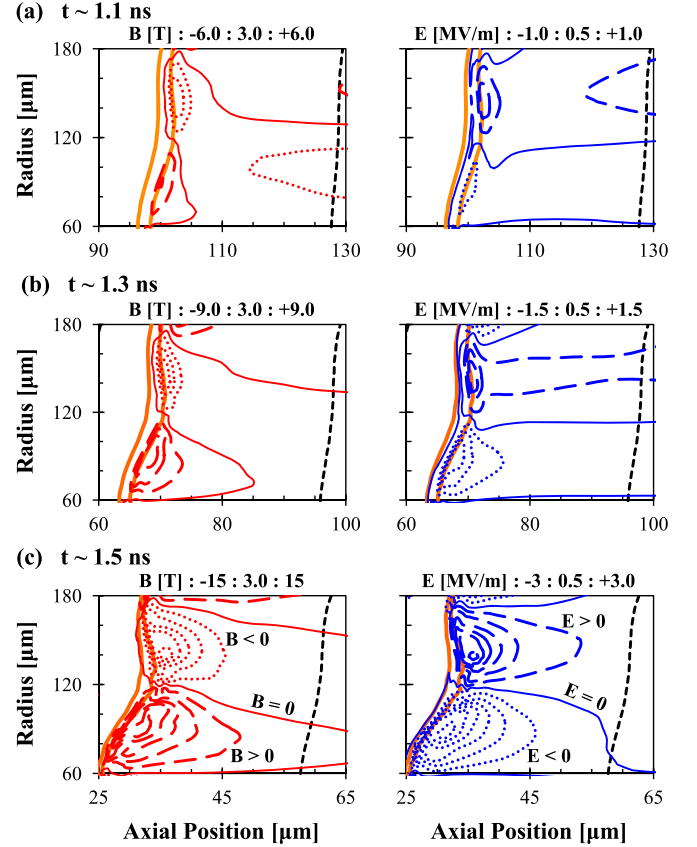

FIG. 4. B-field (left column) and E-field (right column) contour plots calculated from hydrodynamic DRACO simulations. Contour levels are identified at the top of each plot, where negative (in to page) contours are dotted, positive (out of page) contours are long-dashed, and the zero contour is a thin solid line. Peak electron number density contours of 2.5×10^{23} cm^{-3} (thick solid) and the critical surface (short dash) from Figure 3 are shown for spatial reference. Calculations are shown for times from Figure 3: (a) 1.1 ns, (b) 1.3 ns, and (c) 1.5 ns. B and E fields are generated near the ablation surface and are predicted to grow in time.

V. FOURIER ANALYSIS TECHNIQUE

The features of interest in this work are linear perturbations to the proton fluence on a scale length near the wavelength seeded on the foil. A Fourier treatment is used to analyze proton fluence radiographs that are produced from digital scans of the CR-39. In this form, each pixel of the image has a value corresponding to the number of protons incident per unit area, i.e., proton fluence. X-ray radiographs are made from digital scans of the exposed film where each pixel value corresponds to the optical depth measured. Lineouts are taken to quantitatively analyze amplitude modulations in proton fluence and optical depth.

To demonstrate the robustness and fidelity of this process, the analysis of a synthetic image of 120 μm wavelength modulations is illustrated in Figure 5. The image was generated with a known sinusoidal amplitude of 0.05 and mean of 1 ($\alpha_{rms} = 0.035$) oriented at an angle $\theta = 120°$ relative to the horizontal as shown in Figure 5(a). White noise with an amplitude of ± 0.5 was added to illustrate an image with a 0.1 signal-to-background ratio. The lineout along the wave vector, corresponding to an angle of $\theta = 120°$, is shown. Amplitude modulation measurements (α_{rms}) were made from lineouts taken in 10° increments from 0° to 180°, as
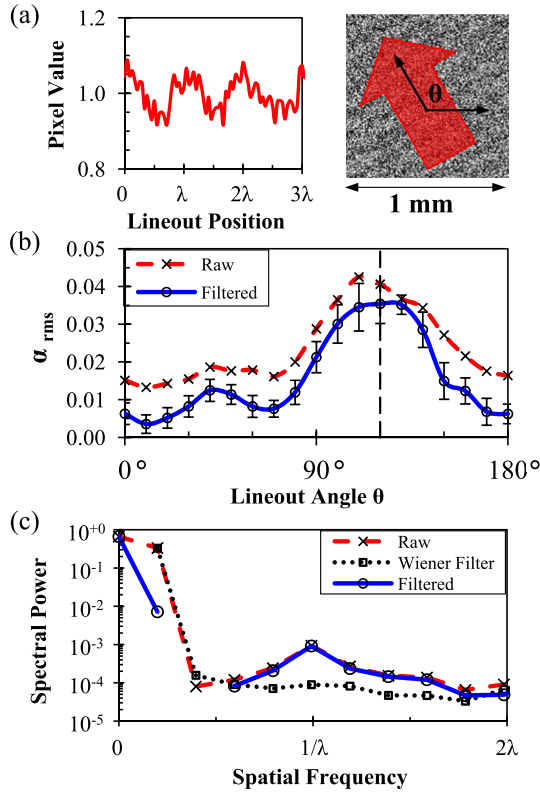
FIG. 5. (a) Lineout of a synthetic image generated with a 0.1 signal-to-noise ratio. The modulation wave vector was angled at $\theta = 120°$ as indicated in the image. (b) Measured rms amplitude modulation at the fundamental frequency as a function of lineout angle for both Raw (dashed) and Filtered (solid) data. (c) Power spectra of the lineout taken at $\theta = 120°$ for both Raw (dashed) and Filtered (solid) data. A Wiener filter (dotted) was constructed as the mean of power spectra taken at angles between 0° and 30°.

illustrated in Figure 5(b). Modulation amplitudes at the specified wavelength are shown to flatten as the lineout orientation becomes perpendicular to the wave vector, as would be expected. For this reason, a clear peak in amplitude modulation is observed at 120° in Figure 5(b).

A DFT of each lineout provides the power density spectrum. A sample spectrum from the lineout shown in Figure 5(a) is shown in Figure 5(c). The frequency of interest is the fundamental frequency $(1/\lambda)$ as derived from the known perturbation wavelength. The amount of amplitude modulation at a spatial frequency f is proportional to the square root of the power density at that frequency,[48,49] $\alpha_f \propto \sqrt{P_f}$. To optimize the accuracy of the spectral power, a Hann-windowing function is used in the DFT to avoid power leakage and the Nyquist frequency is set such that the fundamental frequency is centered on a DFT bin, as illustrated in Figure 5(c). To compare different radiographs, the normalized rms amplitude modulation $\alpha_{\rm rms}$ is defined relative to the background at zero-frequency P_0 (DC offset) as $\alpha_{\rm rms} \equiv \sqrt{P_f/P_0}$. This metric quantifies the rms of a sinusoid at frequency f relative to the mean and is plotted in Figure 5(b) for the synthetic image.

A range of angles near perpendicular to the wavevector are deduced from the "Raw" amplitude modulation ($\times$) measurements in Figure 5(b) and used to calculate an average noise spectrum. In this example, lineouts at angles from

0° to 30° were averaged to generate a Weiner-filter,[48] or estimated noise spectrum, and is shown (dotted) in Figure 5(c). The sample spectrum shown for $\theta = 120°$ clearly demonstrates that the power at the fundamental frequency is well above the noise, even for a 0.1 signal-to-noise ratio.[49] This filter was applied[48] to power spectra at all angles and the corresponding "Filtered" amplitude modulation was calculated and is shown ($\circ$) in Figure 5(b). The implemented rms modulation for this synthetic image was 0.035 and the filtered measurements indicate an rms amplitude of $\alpha_{\rm rms} = 0.035 \pm 0.006$ at the correct wave vector angle of 120°.

Errors in amplitude modulation measurements are primarily due to statistical variations in the image. When calculating a lineout, as seen in Figure 5(a), pixels perpendicular to the lineout direction are averaged. The standard deviation of the mean pixel value is the uncertainty at each point along the lineout. These uncertainties are propagated through the DFT in the manner described by Fornies-Marquina et al.,[50–52] resulting in an uncertainty Δ in the $\alpha_{\rm rms}$ measurement due to statistical variation. If the lineout is wide, this error can be quite small and does not capture the true uncertainty in the $\alpha_{\rm rms}$ analysis.

Amplitude modulation measurements are calculated from a number (S) of thinner sections within the overall lineout envelope. A single $\alpha_{{\rm rms},i}$ is calculated for each section with an uncertainty Δ_i and the total $\alpha_{\rm rms}$ value is obtained as the weighted average

$$\alpha_{\rm rms} = \frac{\sum_i^S \dfrac{\alpha_{{\rm rms},i}}{\Delta_i}}{\sum_i^S \dfrac{1}{\Delta_i}} , \qquad (14)$$

with a statistical uncertainty

$$\Delta_N = \frac{S}{\sum_i^S \dfrac{1}{\Delta_i}} . \qquad (15)$$

The standard deviation of the mean is calculated from the $\alpha_{{\rm rms},i}$ measurements and characterizes the variation in the DFT across the lineout, Δ_{DFT}. The uncertainties are added in quadrature and represent the total error, $\Delta\alpha_{\rm rms} = \sqrt{\Delta_{DFT}^2 + \Delta_N^2}$, in the measurement of a single lineout. This procedure is used on every lineout and the uncertainties in the sample case are illustrated by the error bars in Figure 5(b) at each angle.

VI. EXPERIMENTAL RESULTS

A summary of x-ray and proton radiographic results are shown in Figure 6. Sample x ray radiographs[51] are shown in Figure 6(a) at 1.2, 1.3, and 1.5 ns after the onset of the 2 ns laser drive. X-ray radiographs provided areal density modulations and were used with the mass ablation rate of $\dot{m} \approx 4 \times 10^5 \, {\rm g/cm^2/s}$ to generate the lineouts shown in Figure 6(b) that illustrate mass ablation and perturbation growth. The rms areal densities ($\langle \rho L \rangle_{\rm rms}$) were calculated from these
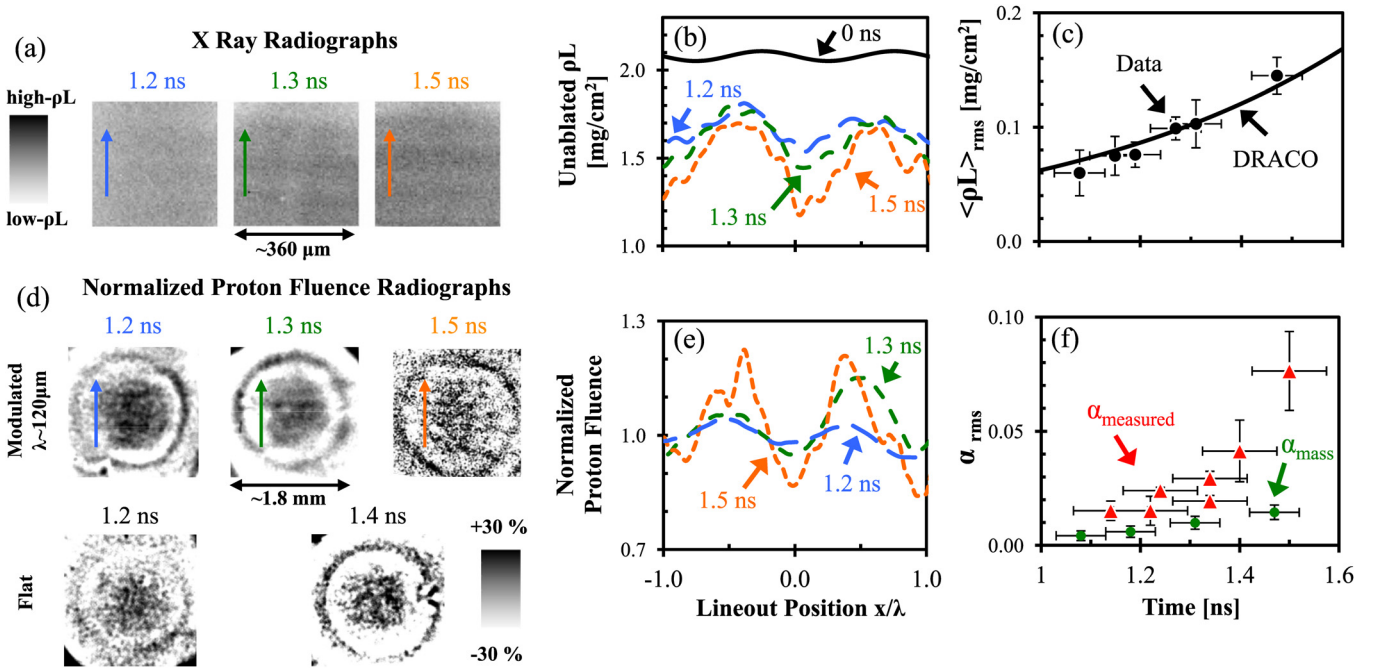
FIG. 6. (a) Sample x-ray radiographs at three times relative to the 2 ns laser drive; scale size is given in the target plane and the lineout direction is indicated. (b) Inferred areal density lineouts from the radiographs shown in (a). The nominal value for 0 ns is shown for comparison. (c) Measured rms areal densities (•) from x-ray radiographs and predicted values (solid) from DRACO. (d) Sample proton fluence radiographs at similar times as x ray images in (a); scale size is given in the target plane and lineout direction is indicated. Flat foil radiographs are shown for comparison. (e) Corresponding lineouts for modulated-foil radiographs in (d) are normalized for comparison across different shots. (f) Measured rms fluence variations (▲) in proton radiographs. Expected rms variation due to mass only (•) was calculated using density distributions from x-ray data.

data and plotted in Figure 6(c). Predicted areal density modulations from DRACO[42] were benchmarked with x ray radiographs as shown by the solid line in Figure 6(c). An exponential fit to $\langle \rho L \rangle_{\mathrm{rms}}$ measurements, independent of simulations, indicates linear growth up to $t \sim 1.5$ ns with a growth rate of $\gamma \approx 2.2$ ns^{-1}.

Proton radiographs of modulated foils were taken over the course of three different shot days, providing data at multiple times during plasma evolution. Figure 6(d) shows sample proton fluence radiographs[52] corresponding to similar times as sample x-ray radiographs shown in Figure 6(a). The visible ring structure in all images illustrates the edge of the laser spot. Within the laser spot, irradiation is uniform and steady RT growth is expected; this inner region is used for analysis. During the times sampled, coherent linear features are observed in modulated-foil proton radiographs. However, radiographs of flat foils at similar times reveal stochastic characteristics in comparison. Lineouts from modulated-foil radiographs are normalized for comparison across different experiments and shown in Figure 6(e).

All radiographs were analyzed using the DFT techniques discussed in Sec. V. The resultant amplitude modulation in proton fluence was found to grow during the 2 ns drive and is shown (▲) in Figure 6(f). It is expected that proton fluence modulations at the fundamental frequency will grow in time due simply to the increase in Coulomb scattering experienced by protons traversing RT spikes as indicated (•) in Figure 7(a). This contribution to α_{rms} was calculated by implementing areal density distributions derived from x-ray radiographs into a simulation[33] written using the Geant4[53] framework. The expected proton fluence amplitude modula-

tions due to mass alone are shown in Figure 6(f) to be 3–5 times less than measured values.

The total amplitude modulation observed in proton fluence is due to a combination of perturbing effects from both field deflections and Coulomb scattering, $\alpha_{\mathrm{rms}}^2 = \alpha_{B/E}^2 + \alpha_{mass}^2$. The Coulomb scattering component was assessed from the x-ray inferred density modulations and shown to be much smaller than the measurements as illustrated in Figure 6. An exponential fit to the calculated α_{mass} values is shown in Figure 7(a).

The contribution to α_{rms} due to scattering was removed, and the residual was attributed to deflections due to RT-induced magnetic and/or electric fields, $\alpha_{B/E} = \sqrt{\alpha_{\mathrm{rms}}^2 - \alpha_{mass}^2}$. During linear growth, a sinusoidally varying field structure develops, as discussed in Sec. IV and demonstrated in Figure 4, which causes sinusoidal deflections. Expected $\alpha_{B/E}$ values were found to be linearly proportional to the rms deflection angle ($\alpha_{B/E} \propto \langle \theta \rangle_{\mathrm{rms}}$) as shown in Figure 7(b). Protons were modeled in the experimental geometry with sinusoidal deflections occurring at the target,

$$\theta = \langle \theta \rangle_{\mathrm{rms}} \sqrt{2} \sin(k_y y), \tag{16}$$

where $\langle \theta \rangle_{\mathrm{rms}}$ is directly proportional to the rms path-integrated field strength for monoenergetic protons. In this way, rms magnetic fields ($\langle BL \rangle_{\mathrm{rms}}$) or electric fields ($\langle EL \rangle_{\mathrm{rms}}$) were inferred from proton fluence modulation measurements. Residual amplitude modulations were attributed to *only magnetic fields* (Figure 8(a)) or *only electric fields* (Figure 8(b)).

Ideal MHD calculations were performed to determine whether B- *or* E-fields dominated proton deflections at the
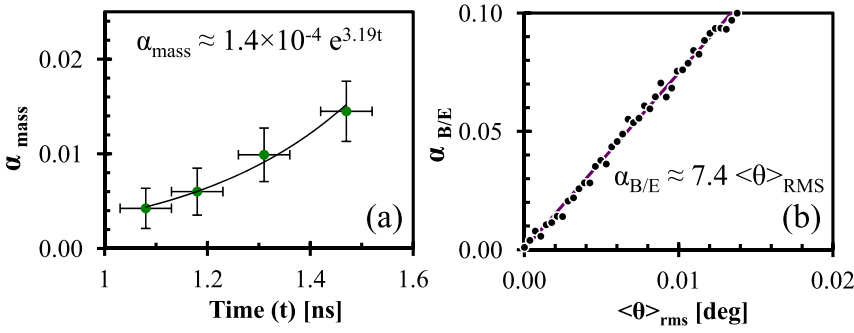
FIG. 7. (a) Amplitude modulation due to x-ray-measured areal density modulations as a function of time (•) with an exponential fit. (b) Modeled amplitude modulation caused by sinusoidal deflection angles at the target (•) with a linear fit.

target. Hydrodynamic calculations from DRACO were post-processed to compute B- and E-field structure as shown in Figure 4. Fields were path-integrated from peak density to the critical surface and the rms value was calculated at each time step. The results of these calculations were compared with the experimentally determined values as shown by the solid lines in Figures 8(a) and 8(b). Even in the ideal limit, E fields are predicted to be $\sim$100 times too small to account for the observed proton deflections. B fields, on the other hand, were predicted to be a factor of $\sim$2 too high to explain the observations; this discrepancy is considered further in Sec. VII. Therefore, it was magnetic, not electric, fields which were responsible for the large fluence modulations observed in proton radiographs.

VII. DISCUSSION

Measurements deduced from proton radiographs are inherently path-integrated quantities. Because of the complexity of the environments they are traversing, inversion techniques are difficult, if not impossible, to apply. Therefore, to estimate magnetic field strengths from path-integrated measurements shown in Figure 8(a), some knowledge of the scale size of these field structures is needed.

The natural scale size of RT-induced fields is the perturbation height.[26] This claim is verified by the contour plots shown in Figures 4(a)–4(c). From these calculations, it is

observed that the spatial extent of the fields grow in time along with the perturbation due to RT growth. The highest field-strength contours are found near the ablation surface and are comparable in width to the peak-to-valley (P-V) perturbation height. Using the initial P-V height ($h_0 \approx 0.54\,\mu m$) and the experimentally determined growth rate, $\gamma_{RT} \approx 2.2\,ns^{-1}$, from Sec. VI, the perturbation height as a function of time can be estimated as $h \approx h_0 e^{\gamma_{RT} t}$. Subsequently, the B field amplitude may be estimated from path-integrated measurements by $B_{max} \approx \sqrt{2}\langle BL\rangle_{rms}/h$.

Resultant B-field amplitude estimates are illustrated (▲) in Figure 9 along with predictions (solid line) from the ideal MHD model. B-field locations inferred from Figure 4 indicate that, at these times, B fields occupy the dense ($n_e \sim 9 \times 10^{22}\,cm^{-3}$), cold ($T_e \sim 300\,eV$) region near the ablation front. Using these plasma conditions in Eq. (2) and the B-field estimates from Figure 9, it was found that thermal conduction will be "reduced" to $\sim$99.7% of its classical value; a negligible effect. Moreover, under these conditions, the predicted plasma β is shown in Figure 9 to be $\gtrsim 10^4$ during the observation times, validating the no-field assumption implemented in the hydrodynamic simulations. If the scale size assumed was too large, and the B field amplitudes were actually higher (within factors of a few) than estimated, the effect on thermal conduction under these plasma conditions is still minimal due to the high collisionality near the ablation front.
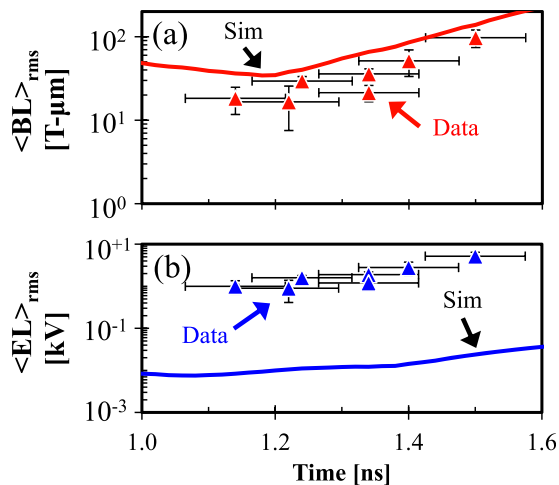

FIG. 8. Inferred path-integrated quantities (▲) are calculated from measured α_{rms} values if deflections are caused by (a) B-fields and mass, or (b) E-fields and mass. Simulated B fields indicate an approximate upper estimate and are a factor of $\sim$2 higher than inferred values, whereas simulated E fields are a factor of $\sim$100 too low to account for measured proton fluence modulations.
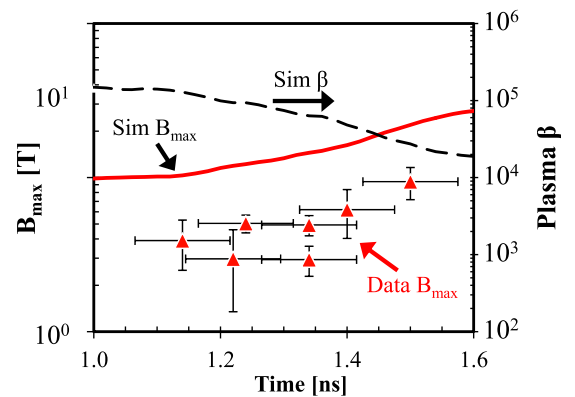

FIG. 9. Estimated B field amplitudes (▲) inferred from path-integrated measurements. The field structure scale length is the perturbation height as determined by the experimentally determined growth rate and initial foil conditions. B field amplitudes predicted by the ideal MHD model are shown (solid) for comparison. The predicted plasma β is also shown using the ablation parameters $n_e \sim 9 \times 10^{22}\,cm^{-3}$ and $T_e \sim 300\,eV$.

These measurements indicate a negligible effect on electron thermal conduction due to B fields under the specified target and laser conditions. However, it is clear from the ideal calculations illustrated in Figure 4 that the B field structure grows in time and begins to extend toward the critical surface. As RT growth continues into the non-linear regime, the spikes will "fall" closer to the critical surface generating fields[23] further away from the ablation front. Plasma conditions near the critical surface ($n_{cr} \sim 10^{22}$ cm^{-3} and $T_e \sim 800$ eV) are different than those at the ablation front and in this environment a B field of ~ 10 T can reduce thermal conduction to $\sim 80\%$ of its classical value. Although, in B-field calculations presented herein, Nernst[47,54] convection and diffusion effects were neglected due to computational constraints and may alter the B-field dynamics.

Nernst convection ($\mathbf{V}_T$) is a collisional effect due to temperature gradients in the plasma that cause the fluid to convect with the heat flow ($\mathbf{q}$), as $\mathbf{V}_T \propto \mathbf{q} \propto -\nabla T$. In the over dense region, Nernst convection flows away from the critical surface and towards the ablation front. Therefore, any magnetic fields that are generated closer to the critical surface will feel an additional convective force towards the ablation front. As magnetic fields are convected toward the denser, colder regions of the ablation front, the local resistivity increases and magnetic diffusion may play a bigger role in the dynamics. The field amplification typically[54] associated with Nernst convection in this region will no longer hold near the ablation front. With higher resistivity, the frozen-in mechanism causing the amplification is no longer present. The field diffusion time can be approximated as

$$\tau_{diff} \approx \frac{\mu_0}{\eta k^2} , \qquad (17)$$

where η is the resistivity and k is the wavenumber. At ~ 300 eV temperatures in this plasma, $\tau_{diff} \sim 1$ ns which is of the same order as the RT-growth time scale. Measurements shown in Figure 8(a) were consistently lower than the ideal calculations, suggesting that diffusion of B fields into the colder, denser plasma may be occurring.

Collisional effects causing magnetic field diffusion are contained in the $\mathbf{R}_e$ term in Eq. (9). Inclusion of the frictional force reveals the diffusion mechanism in the B field evolution equation,

$$\frac{\partial \mathbf{B}}{\partial t} \approx \nabla \times \left(\frac{\nabla p_e}{e_0 n_e} \right) + \nabla \times (\mathbf{V}_i \times \mathbf{B}) + D_m \nabla^2 \mathbf{B} , \qquad (18)$$

where D_m is the constant magnetic diffusion coefficient and is related to the plasma resistivity by $D_m = \eta/\mu_0$. To estimate the reduction in field strength due to diffusive effects, a simple correction factor[25] may be used in Eq. (13),

$$\mathbf{B} \approx \frac{1}{1 + \frac{k^2 D_m}{\gamma_{RT}}} \frac{-m_i}{e_0(Z+1)} \boldsymbol{\xi} , \qquad (19)$$

where k is the wavenumber of the perturbations under investigation and γ_{RT} is the growth rate. Using this formalism with the experimentally determined RT growth rate and assuming

the plasma temperature near the ablation front is ~ 300 eV, this calculation results in a correction factor of ~ 0.4 implying that the ideal calculation overestimates the field magnitude by ~ 2.5 times. A correction of this magnitude would account for the discrepancy observed between the experimental data and the ideal predictions illustrated in Figure 8(a).

The magnetic Reynolds number is a fundamental parameter used to determine the importance of diffusion in a conducting fluid. It is defined as $\text{Re}_m = VL/D_m$, where V is the flow velocity and L is the scale length. Assuming that the flow is relatively constant (to within factors of a few) at $\sim 150 \, \mu\text{m/ns}$, and that the scale length is determined[55] by the temperature gradients as shown in Figure 3, the magnetic Reynolds numbers at various locations were estimated: near the ablation front, $\text{Re}_m \sim 0.1$; at the critical surface, $\text{Re}_m \sim 50$; and at the quarter critical surface (in the corona), $\text{Re}_m \sim 2000$. As the plasma becomes hotter and more homogenous (longer scale lengths), diffusion becomes less important and the B fields are "frozen" in the plasma. However, RT-generated fields occur near the ablation surface where $\text{Re}_m < 1$ and diffusion will play a bigger role.

VIII. CONCLUSION

Path-integrated measurements of RT-induced magnetic fields were made using a combination of x-ray and proton radiographic techniques. Experiments were performed using planar targets with initial surface perturbations at a wavelength of $\lambda \sim 120 \, \mu\text{m}$. Field-strength information was encoded within proton fluence modulations due to the relationship between the deflection of a monoenergetic proton beam and the path-integrated field strength. Radiographs were analyzed using a discrete-Fourier-transform technique to recover data at the known wavelength of interest. X-ray measurements provided experimental density modulations at the target and a growth rate of 2.2 ns^{-1} was inferred. Density modulations were shown to contribute very little to the overall amplitude modulation observed in proton fluence radiographs and field strengths were inferred.

Amplitude modulation in proton radiographs was shown to be dominated by magnetic deflections. Path-integrated measurements exhibited an increase from ~ 10 T-μm to ~ 100 T-μm during linear growth. These path-integrated measurements correspond to estimated field strengths of ~ 2 to ~ 10 T. Radiation-hydrodynamic simulations done with DRACO were post-processed to calculate magnetic field structures in the ideal MHD limit for comparison with data. In this limit, B fields were shown to be proportional to fluid vorticity and due to the high ($\gtrsim 10^4$) plasma beta, do not affect the bulk hydrodynamics. Path-integrated B-field measurements were found to be a factor of ~ 2 lower than ideal predictions. In these calculations, B-fields were shown to be generated near the ablation front, where plasma conditions allow for higher resistivity. In this environment, diffusion will play a larger role in the dynamics, thereby reducing the B-field strength in the experiment relative to the ideal calculations. Using a simple correction factor to the ideal model, it was shown that diffusive effects in these experiments would account for the observed discrepancy.

Under the plasma and laser conditions explored in these experiments, RT-induced B fields due to 120-μm wavelength perturbations were shown to have a negligible effect on electron thermal conduction. B fields generated near the ablation front will, in general, have a minimal effect on thermal conduction due to the high collisionality in that region. Furthermore, Nernst convection will act to push these fields into the colder, denser plasma where resistivity is higher and diffusion may more readily occur. Of greater concern are B fields created by non-linear RT where generation may occur closer to the critical surface and inhibition of thermal conduction may take place at lower B-field magnitudes.

Experiments are currently planned to investigate RT-induced magnetic fields during non-linear growth using x-ray and proton radiography. Work is also being done to acquire simulations for these experiments with full consideration of diffusive and convective effects.

ACKNOWLEDGMENTS

[1] J. W. Strutt, "Investigation of the character of the equilibrium of an incompressible heavy fluid of variable density," Proc. London Math. Soc. **14**(1), 8 (1883).

[2] G. Taylor, "The instability of liquid surfaces when accelerated in a direction perpendicular to their planes," Proc. R. Soc. London **201**(1065), 192 (1950).

[3] J. Nuckolls, L. Wood, A. Thiessen *et al.*, "Laser compression of matter to super-high densities: Thermonuclear (CTR) applications," Nature **239**, 139 (1972).

[4] S. W. Haan, "Onset of nonlinear saturation for Rayleigh-Taylor growth in the presence of a full spectrum of modes," Phys. Rev. A **39**(11), 5812 (1989).

[5] H. Takabe, K. Mima, L. Montierth *et al.*, "Self-consistent growth rate of the Rayleigh–Taylor instability in an ablatively accelerating plasma," Phys. Fluid **28**(12), 3676 (1985).

[6] R. Betti, V. N. Goncharov, R. L. McCrory *et al.*, "Growth rates of the ablative Rayleigh–Taylor instability in inertial confinement fusion," Phys. Plasmas **5**(5), 1446 (1998).

[7] S. E. Bodner, "Rayleigh-Taylor instability and laser-pellet fusion," Phys. Rev. Lett. **33**(13), 761 (1974).

[8] B. A. Remington, S. V. Weber, M. M. Marinak *et al.*, "Multimode Rayleigh-Taylor experiments on nova," Phys. Rev. Lett. **73**(4), 545 (1994).

[9] J. P. Knauer, R. Betti, D. K. Bradley *et al.*, "Single-mode, Rayleigh-Taylor growth-rate measurements on the OMEGA laser system," Phys. Plasmas **7**(1), 338 (2000).

[10] V. A. Smalyuk, S. X. Hu, V. N. Goncharov *et al.*, "Systematic study of Rayleigh–Taylor growth in directly driven plastic targets in a laser-intensity range from $\sim$2×10^{14} to $\sim$1.5×10^{15} W/cm^2," Phys. Plasmas **15**(8), 082703 (2008).

[11] S. G. Glendinning, S. V. Weber, P. Bell *et al.*, "Laser-driven planar Rayleigh-Taylor instability experiments," Phys. Rev. Lett. **69**(8), 1201 (1992).

[12] J. A. Stamper, K. Papadopoulos, R. N. Sudan *et al.*, "Spontaneous magnetic fields in laser-produced plasmas," Phys. Rev. Lett. **26**(17), 1012 (1971).

[13] M. G. Haines, "Magnetic-field generation in laser fusion and hot-electron transport," Can. J. Phys. **64**(8), 912 (1986).

[14] R. G. Evans, "The influence of self-generated magnetic fields on the Rayleigh-Taylor instability," Plasma Phys. Controlled Fusion **28**(7), 1021 (1986).

[15] All experiments discussed here used plastic foils with an atomic ratio of 1 carbon to 1.38 hydrogens.

[16] S. I. Braginskii, "Transport processes in a plasma," in *Reviews of Plasma Physics* (Consutants Bureau, New York, 1965), Vol. 1.

[17] J. D. Lindl, P. Amendt, R. L. Berger *et al.*, "The physics basis for ignition using indirect-drive targets on the National Ignition Facility," Phys. Plasmas **11**(2), 339 (2004).

[18] C. C. Joggerst, A. Almgren, and S. E. Woosley, "Three-dimensional simulations of Rayleigh-Taylor mixing in core-collapse supernovae," Astrophys. J. **723**, 11 (2010).

[19] H. Isobe, T. Miyagoshi, K. Shibata *et al.*, "Filamentary structure on the Sun from the magnetic Rayleigh-Taylor instability," Nature **434**(7032), 478 (2005).

[20] G. Gregori, A. Ravasio, C. D. Murphy *et al.*, "Generation of scaled protogalactic seed magnetic fields in laser-produced shock waves," Nature **481**(7382), 480 (2012).

[21] A. Schluter and L. Biermann, "Interstellar magnetic fields," Z. Naturforsch. A **5**, 237 (1950).

[22] B. Fryxell, C. C. Kuranz, R. P. Drake *et al.*, "The possible effects of magnetic fields on laser experiments of Rayleigh-Taylor instabilities," High Energy Density Phys. **6**(2), 162 (2010).

[23] B. Srinivasan, G. Dimonte, and X. Tang, "Magnetic field generation in Rayleigh-Taylor unstable ICF plasmas," Phys. Rev. Lett. **108**(16), 165002 (2012).

[24] K. Mima, T. Tajima, and J. N. Leboeuf, "Magnetic field generation by the Rayleigh-Taylor instability," Phys. Rev. Lett. **41**(25), 1715 (1978).

[25] A. Nishiguchi, "Effects of self-generated magnetic field on Rayleigh-Taylor instability," Jpn. J. Appl. Phys., Part 1 **41**(1), 326 (2002).

[26] M. J.-E. Manuel, C. K. Li, F. H. Séguin *et al.*, "First measurements of Rayleigh-Taylor-induced magnetic fields in laser-produced plasmas," Phys. Rev. Lett. **108**(25), 255006 (2012).

[27] P. B. Radha, V. N. Goncharov, T. J. B. Collins *et al.*, "Two-dimensional simulations of plastic-shell, direct-drive implosions on OMEGA," Phys. Plasmas **12**(3), 032702 (2005).

[28] T. R. Boehly, D. L. Brown, R. S. Craxton *et al.*, "Initial performance results of the OMEGA laser system," Opt. Commun **133**(1–6), 495 (1997).

[29] V. A. Smalyuk, T. R. Boehly, D. K. Bradley *et al.*, "Characterization of an x-ray radiographic system used for laser-driven planar target experiments," Rev. Sci. Instrum, **70**(1), 647 (1999).

[30] V. A. Smalyuk, "Experimental investigation of the nonlinear Rayleigh-Taylor instability in CH foils irradiated by UV light," Ph.D. dissertation (University of Rochester, 1999).

[31] C. K. Li, F. H. Séguin, J. A. Frenje *et al.*, "Proton radiography of dynamic electric and magnetic fields in laser-produced high-energy-density plasmas," Phys. Plasmas **16**(5), 056304 (2009).

[32] C. K. Li, F. H. Séguin, J. A. Frenje *et al.*, "Measuring E and B fields in laser-produced plasmas with monoenergetic proton radiography," Phys. Rev. Lett. **97**(13), 135003 (2006).

[33] M. J.-E. Manuel, A. B. Zylstra, H. G. Rinderknecht *et al.*, "Source characterization and modeling development for monoenergetic-proton radiography experiments at OMEGA," Rev. Sci. Instrum. **83**(6), 063506 (2012).

[34] F. H. Séguin, C. K. Li, M. J.-E. Manuel *et al.*, "Time evolution of filamentation and self-generated fields in the coronae of directly driven inertial-confinement fusion capsules," Phys. Plasmas **19**(1), 012701 (2012).

[35] J. R. Rygg, F. H. Séguin, C. K. Li *et al.*, "Proton radiography of inertial fusion implosions," Science **319**(5867), 1223 (2008).

[36] C. K. Li, F. H. Séguin, J. R. Rygg *et al.*, "Monoenergetic-proton-radiography measurements of implosion dynamics in direct-drive inertial-confinement fusion," Phys. Rev. Lett. **100**(22), 225001 (2008).

[37] R. D. Petrasso, C. K. Li, F. H. Séguin *et al.*, "Lorentz mapping of magnetic fields in hot dense plasmas," Phys. Rev. Lett. **103**(8), 085001 (2009).

[38] F. H. Séguin, J. A. Frenje, C. K. Li *et al.*, "Spectrometry of charged particles from inertial-confinement-fusion plasmas," Rev. Sci. Instrum. **74**(2), 975 (2003).

[39] Y. Lin, T. J. Kessler, and G. N. Lawrence, "Distributed phase plates for super-Gaussian focal-plane irradiance profiles," Opt. Lett. **20**(7), 764 (1995).

[40] S. P. Regan, J. A. Marozas, J. H. Kelly *et al.*, "Experimental investigation of smoothing by spectral dispersion," J. Opt. Soc. Am. B **17**(9), 1483 (2000).

[41] T. R. Boehly, V. A. Smalyuk, D. D. Meyerhofer *et al.*, "Reduction of laser imprinting using polarization smoothing on a solid-state fusion laser," J. Appl. Phys. **85**(7), 3444 (1999).

[42]D. Keller, T. J. B. Collins, J. A. Delettrez *et al.*, "DRACO—A new multi-dimensional hydrocode," 41st Annual Meeting of the Division of Plasma Physics in Seattle, WA (1999).

[43]V. A. Smalyuk, S. X. Hu, J. D. Hager *et al.*, "Rayleigh-Taylor growth measurements in the acceleration phase of spherical implosions on OMEGA," Phys. Rev. Lett. **103**(10), 105001 (2009).

[44]R. C. Malone, R. L. McCrory, and R. L. Morse, "Indications of strongly flux-limited electron thermal conduction in laser-target experiments," Phys. Rev. Lett. **34**(12), 721 (1975).

[45]C. K. Li, F. H. Séguin, J. A. Frenje *et al.*, "Charged-particle probing of X-ray-driven inertial-fusion implosions," Science **327**(5970), 1231 (2010).

[46]M. Borghesi, D. H. Campbell, A. Schiavi *et al.*, "Electric field detection in laser-plasma interaction experiments via the proton imaging technique," Phys. Plasma **9**(5), 2214 (2002).

[47]A. Nishiguchi, T. Yabe, M. G. Haines *et al.*, "Convective amplification of magnetic fields in laser-produced plasmas by the Nernst effect," Phys. Rev. Lett. **53**(3), 262 (1984).

[48]W. H. Press, S. A. Teukolsky, W. T. Vetterling *et al.*, *Numerical Recipes in c^{++}: The Art of Scientific Computing*, 2nd ed. (Cambridge University Press, 2002).

[49]Raw powers below the noise are set to zero and not shown on the log scale.

[50]J. M. Fornies-Marquina, J. Letosa, M. Garcia-Gracia *et al.*, "Error propagation for the transformation of time domain into frequency domain," IEEE Trans. Magn. **33**(2), 1456 (1997).

[51]X ray radiographs were from OMEGA shot 50870.

[52]Sample proton radiographs were from OMEGA shots 49109 (1.2 ns), 61721(1.3 ns), 49111(1.5 ns) for modulated foils and 50610 (1.2 ns), 50610 (1.4 ns) for flat foils.

[53]J. Allison, K. Amako, J. Apostolakis *et al.*, "Geant4 developments and applications," IEEE Trans. Nucl. Sci. **53**(1), 270 (2006).

[54]A. Nishiguchi, T. Yabe, and M. G. Haines, "Nernst effect in laser-produced plasmas," Phys. Fluids **28**(12), 3683 (1985).

[55]C. K. Li, F. H. Séguin, J. A. Frenje *et al.*, "Observation of megagauss-field topology changes due to magnetic reconnection in laser-produced plasmas," Phys. Rev. Lett. **99**(5), 055001 (2007).